



Nanoscale

Polymer-infiltrated Nanoplatelet Films with Nacre-like Structure via Flow Coating and Capillary Rise Infiltration (CaRI)

Journal:	<i>Nanoscale</i>
Manuscript ID	NR-ART-12-2020-008691.R1
Article Type:	Paper
Date Submitted by the Author:	26-Feb-2021
Complete List of Authors:	Qiang, Yiwei; University of Pennsylvania Turner, Kevin; University of Pennsylvania, Mechanical Engineering and Applied Mechanics Lee, Daeyeon; University of Pennsylvania,

SCHOLARONE™
Manuscripts

Polymer-infiltrated Nanoplatelet Films with Nacre-like Structure *via* Flow Coating and Capillary Rise Infiltration (CaRI)

Yiwei Qiang,^a Kevin T. Turner^{a,b} and Daeyeon Lee^c

^aDepartment of Materials Science and Engineering, ^bDepartment of Mechanical Engineering and Applied Mechanics and ^cDepartment of Chemical and Biomolecular Engineering, University of Pennsylvania, Philadelphia, Pennsylvania 19104, United States

Abstract:

Alignment of highly anisotropic nanomaterials in a polymer matrix can yield nanocomposites with unique mechanical and transport properties. Conventional methods of nanocomposite film fabrication are not well-suited for manufacturing composites with very high concentrations of anisotropic nanomaterials, potentially limiting the widespread implementation of these useful nanocomposite structures. In this work, we present a scalable approach to fabricate polymer-infiltrated nanoplatelet films (PINFs) based on flow coating and capillary rise infiltration (CaRI) and study the processing-structure-property relationship of these PINFs. We show that films with high aspect ratio (AR) gibbsite ($\text{Al}(\text{OH})_3$) nanoplatelets (NPTs) aligned parallel to the substrate can be prepared using a flow coating process. NPTs are highly aligned with a Herman's order parameter of 0.96 and a high packing fraction >80 vol%. Such packings show significantly higher fracture toughness compared to low AR nanoparticle (NP) packings. By depositing NPTs on a polymer film and subsequently annealing the bilayer above the glass transition temperature of the polymer, polymer infiltrates into the tortuous NPT packings through capillarity. We observe larger enhancement in the modulus, hardness and scratch resistance of NPT films upon polymer infiltration compared to NP packings. The excellent mechanical properties of such films benefit from both thermally promoted oxide bridge formation between NPTs as well as polymer infiltration increasing the strength of NPT contacts. Our approach is widely applicable to highly anisotropic nanomaterials and allows the generation of mechanically robust polymer nanocomposite films for a diverse set of applications.

Keywords: anisotropic nanomaterials, flow coating, capillary rise infiltration, ellipsometry, nanoindentation

1. Introduction

Advances in the synthesis strategies for nanomaterials have led to the development of a broad range of anisotropic nanomaterials including nanowires, nanotubes, nanorods, nanoellipsoids, nanodumbbells, nanoplatelets and many more.^{1,2} Anisotropic nanomaterials are versatile building blocks for advanced functional materials due to their shape and unique optical, electric, magnetic and mechanical properties.³⁻⁹ Incorporating a high loading of anisotropic nanomaterials (>50 vol%) into a polymer matrix yields nanocomposites with unique mechanical and transport properties.¹⁰ For example, polymer nanocomposites with a high volume fraction of 2D nanosheets are promising candidates as electrodes for energy storage devices due to efficient charge transport and high mechanical stability.^{11,12} Highly loaded polymer nanocomposites based on conductive nanofillers, such as carbon nanotubes (CNTs) and boron nitride (BN) nanoplatelets, achieve high thermal conductivity by creating percolated pathways for phonon transport.^{13,14}

One of the key challenges in fabricating polymer nanocomposites with anisotropic nanomaterials is the difficulty associated with handling and processing mixtures of polymer and such nanofillers. Conventional methods such as melt compounding requires high temperatures to blend nanofillers and polymer and also suffer from low flowability at high loading levels.^{10,14} Solution mixing, in which nanofillers are dispersed in polymer solutions, generally requires organic solvents and the resulting composition is limited by the dispersion limit of the nanofillers.¹³ These problems are generally exacerbated when anisotropic nanomaterials are used due to very high viscosity of the composites even at modest loading levels.¹⁵ Another challenge associated with anisotropic nanomaterials is that controlled alignment of these nanomaterials is necessary to fully harness their unique properties. For example, in organic-inorganic heterojunction photovoltaic devices based on CdSe nanorods, vertically oriented nanorods can maximize the carrier transport distance and improve device performance.¹⁶ Polymer nanocomposites with direction-dependent thermal properties have high potential in thermal management applications and also rely on alignment of nanofillers.^{17,18}

Scaffold impregnation is an alternative approach to synthesize nanocomposites that overcomes many of the limitations of conventional methods. In this process, a scaffold is fabricated first and then subsequently filled by polymer infiltration.¹⁰ The resulting nanocomposites are generally very dense and the process provides good control over filler alignment. Polymer infiltration is a critical step and can be achieved by several methods such as in-situ polymerization, solution or melt impregnation. However, in-situ polymerization is limited to certain polymers and can be strongly affected under nanoconfinement.¹⁹ Recently, versatile and scalable techniques based on capillarity have been developed to prepare polymer nanocomposite films with extremely high filler fractions.²⁰⁻²³ These techniques can be applied to low glass transition temperature (T_g) or high T_g polymers, at room temperature or high temperature to generate polymer-infiltrated nanoparticle films (PINFs). In a method that we call capillary rise infiltration (CaRI), NP packing/polymer bilayer films are thermally annealed above the T_g of the polymer to induce wicking of the polymer into the pores of the packing.²⁰ When the amount of polymer is less than the void volume in the packing, undersaturated CaRI (UCaRI) films with either homogenous or graded porosity can be fabricated.²¹ By varying polymer volume fraction, the elastic modulus, hardness and fracture toughness of UCaRI films made of TiO_2 nanoparticles and a glassy polymer, polystyrene, could be increased up to $\sim 2.5\times$, $\sim 3.5\times$ and $\sim 9\times$ of the neat NP packing, respectively.^{21,24} In addition to enhancing mechanical properties, PINFs prepared by CaRI have found multiple applications including thermal management,²⁵ oil/water separation,^{26,27} and anticorrosive coatings.²⁸ The simplicity and versatility of CaRI makes it powerful approach for fabricating porous and nonporous functional nanocomposite films with high mechanical robustness.

Our previous work on CaRI nanocomposites has focused on using spherical and low aspect ratio ($AR \leq 6$) ellipsoids.^{20,21,24,29,30} Among a variety of anisotropic nanomaterials, platelet-like particles are particularly interesting due to their capability to assemble into layered structures and form composites that mimic the structure of natural composites such as nacre.³¹ Nacre, the inner layer of mollusk shells, is composed of 95 vol% of brittle CaCO_3 aragonite platelets (lateral dimensions of 5-8 μm , thicknesses of 200-900 nm) as ‘bricks’ and 5 vol% of soft biopolymers (10-50 nm) as ‘mortar’.³²⁻³⁴ The intrinsic brick-and-mortar structure along with other nanoscale features (e.g. nanoasperities and mineral bridges) makes nacre one of the toughest and strongest natural

materials.^{35,36} Moreover, composites based on platelet-like particles often have attractive transport properties, including high thermal conductivity,^{18,37} fire-shielding,^{38,39} and gas barrier properties.^{38,40}

In this work, we present an approach to fabricate polymer nanocomposite films loaded with high volume fractions of well-aligned hexagonal nanoplatelets (NPTs) by flow coating and CaRI. Hexagonal gibbsite ($\text{Al}(\text{OH})_3$) NPTs are selected as the model particle due to well-defined dimensions, excellent colloidal stability and liquid crystalline phase behavior.^{41–43} The assembly of gibbsite NPTs into films with high alignment have been performed using electrophoretic deposition,^{41,42} vacuum filtration⁴⁴ and solution casting⁴⁵; however, these methods are not conducive to scalable manufacturing. Here, we use flow coating, which is a rapid and scalable method for film deposition,^{46,47} to prepare highly-oriented, densely-packed films of gibbsite NPTs. Polymer infiltration into the highly tortuous NPT packing via CaRI is induced by thermally annealing NPT/polymer bilayers. We characterize the elastic modulus, hardness, fracture toughness and scratch resistance of these films and demonstrate that polymer-infiltrated NPT films show excellent mechanical properties. Due to the versatility and scalability of flow coating and CaRI process, our approach can be applied to various anisotropic nanomaterials and enables the generation of mechanically robust polymer nanocomposites films for multiple applications.

2. Materials and methods

2.1 Materials

Gibbsite NPTs are synthesized using a previously described hydrothermal method.⁴⁸ Larger NPTs are obtained with seeded growth procedure. Concentrated gibbsite NPT suspensions are obtained by washing as-synthesized suspensions through centrifugation-redispersion cycles at least 6 times to remove any unreacted precursor and dissolved byproducts. Aluminum sec-butoxide (ASB, 97%) is purchased from Sigma-Aldrich and hydrochloric acid (HCl, 1N) is purchased from Fisher Scientific. Polystyrene 8k ($M_n = 8000 \text{ g mol}^{-1}$, $PDI = 1.10$) is purchased from Polymer Source, Inc. TiO_2 NPs ($2a = 47 \pm 5 \text{ nm}$, $2b = 25 \pm 4 \text{ nm}$) are synthesized using previously reported sol-gel method.⁴⁹

2.2 Fabrication of neat and polymer-infiltrated gibbsite NPT films

Prior to film deposition, Si wafers are cut into approximately $2 \text{ cm} \times 2 \text{ cm}$ squares. The wafers are rinsed with isopropanol and deionized water and dried with nitrogen. Then, the wafers are further cleaned by oxygen plasma treatment for ~ 4 mins. Gibbsite NPTs are deposited on the substrate using a home-built flow coater (Figure S4 and video 1). A glass slide is cleaned with deionized water and serves as the blade. The cleaned substrate is placed on a computer controlled motorized stage (Thorlabs) and moves at a constant velocity, v , along the x -axis. The gap height between the blade and the substrate is set to be $60 \mu\text{m}$ by attaching single-sided tape on the two sides of the substrate and adjusting the blade such that it is in close contact with the tape. The angle between the blade and substrate is set to be 25° . During every deposition, an 8 wt% gibbsite NPT ethanol/water suspension (mass ratio of ethanol to water = 2:1) with a volume of $6 \mu\text{L}$ is confined between the blade and the substrate. Substrate velocity v is varied from 1 mm/s to 9 mm/s to control the thickness of deposited film. To fabricate polymer-infiltrated NPT films, PS films are first

deposited on the cleaned substrate using a WS-400BZ-6NPP/Lite spin coater from Laurell Technologies Corporation. The PS solutions are prepared by dissolving PS in toluene and filtered prior to use. The concentrations of the PS solutions depend on the desired film thickness. To generate 200-250 nm PS films for ellipsometry studies, a 5–6 wt % PS solution is prepared and spin-coated at 2000–2500 rpm. For mechanical tests, thick PS films (>500 nm) require spin-coating a 10 wt % PS solution at 1000–2000 rpm. Then, PS films are oxygen plasma-treated for five seconds to render the surface hydrophilic, on which gibbsite NPTs are flow-coated once or multiple times to form bilayer films with desired thickness. For ellipsometry studies, NPT/PS bilayer films (NPT layer thickness <500 nm) are annealed on a temperature-controlled stage (Linkam Scientific) at 130 or 150 °C, until the interstices in the NPT layer are completely filled with PS via capillary rise infiltration. For mechanical tests, thick bilayer films (NPT layer thickness >2 μm) are annealed in an oven, which is set at 180 °C to achieve rapid infiltration. Neat and polymer-infiltrated TiO₂ NP films are prepared as previously reported.²⁰

2.3 Characterization

2.3.1 Scanning electron microscopy

Scanning electron microscopy (SEM) images of the gibbsite NPT films and gibbsite NPT/PS bilayer films before and after polymer infiltration are taken using a FEI-600 Quanta ESEM. Before imaging, each sample is coated with 4 nm of iridium to prevent charging. The SEM images are captured at an accelerating voltage of 20 kV, a spot size of 3.0 and working distance around 10 mm.

2.3.2 Atomic force microscopy

AFM images of gibbsite NPT film are collected using a Bruker Dimension Icon AFM with a silicon tapping-mode probe. Gwyddion software is used to process the images and extract the thickness of the NPTs (Figure S2).

2.3.3 Zeta potential measurement

Zeta (ζ)-Potential of gibbsite NPTs is measured by a Delsa Nano C particle analyzer at 25 °C using a 0.56 wt% gibbsite aqueous suspension in a clear disposable zeta cell. The Smoluchowski equation is applied in data analysis.⁵⁰

2.3.4 Spectroscopic ellipsometry

The thickness and refractive index of deposited films are measured using spectroscopic ellipsometry (M-2000 V and Alpha-SE, J.A. Woollam). The raw ellipsometry data $\Psi(\lambda)$ and $\Delta(\lambda)$ are fit using Cauchy dispersion relations ($n(\lambda) = A + B/\lambda^2$, $k(\lambda) = 0$), where n and k are the real and imaginary parts of the refractive index. Depending on the sample, either a one-layer (for neat gibbsite NPT films) or two-layer (gibbsite NPT/PS bilayers) model on the Si substrate with 1 nm native oxides is used. The PS layer is fit using an isotropic Cauchy model and the gibbsite NPT layer is fit using an anisotropic Cauchy model to describe the refractive index for the in-plane and out-of-plane directions of the film. For in-situ ellipsometry studies, samples are placed on a

temperature-controlled stage (Linkam Scientific) which is connected to the ellipsometer. A LabVIEW program is used to set the desired temperature, cooling/heating rate and holding time.

2.3.5 UV-vis spectroscopy

The UV-vis spectroscopy (200-800 nm) of neat gibbsite NPT and gibbsite NPT/PS bilayer films is conducted on a Cary 5000 UV-Vis/NIR spectrophotometer (Agilent Technologies). Samples are coated on quartz slides and transmission data are obtained by mounting the slides on the holder such that the films are perpendicular to the beam path.

2.3.6 Grazing incidence wide-angle X-ray scattering (GIWAXS)

GIWAXS characterization of gibbsite NPT films is conducted using a dual source Cu/Mo environmental X-Ray Scattering instrument (Xenocs Xeuss 2.0 at the DEXS facility, University of Pennsylvania). A Cu source ($\lambda = 1.5406 \text{ \AA}$) is used and a 1M Pilatus solid state detector is placed at a distance of 176 mm from the samples. The X-ray exposure time for the samples is 900 s during which the samples are kept under vacuum to reduce scatter from atmospheric gases. Foxtrot software is used to convert the two-dimensional (2D) GIWAXS patterns to q-space, construct one-dimensional (1D) radial intensity profiles and azimuthal intensity profiles across the main peak (002). The diffraction pattern of silver behenate (AgBeh) is used to calibrate the sample-to-detector distance.

2.3.7 X-ray diffraction (XRD)

A powder x-ray diffractometer (XRD) (Rigaku Rigaku D/Max-B diffractometer) is used to analyze the phase composition of synthesized NPTs.

2.3.8 Nanoindentation, nanoscratch and pillar-splitting fracture test

The elastic modulus, hardness, scratch resistance and fracture toughness of neat gibbsite NPT and polymer-infiltrated NPT films ($>2 \text{ \mu m}$ in thickness) are measured using a Hysitron TI 950 TriboIndenter. A diamond Berkovich tip is used and the area function of the tip is calibrated through a series of indents on a fused silica sample. Before all measurements, the thermal drift is stabilized to less than 0.3 nm s^{-1} . For each sample, 25 indentation tests, with 9 partial unloading cycles each, are performed on a 5×5 grid with a spacing of 10 \mu m between the indents. The maximum loads in the test range from 200-300 μN , resulting in indentation depths from 20-250 nm. The hardness and modulus are determined from the load-displacement curves following the Oliver-Pharr method⁵¹ using Triboscan software. Tests with indentation depths in the range of 50-190 nm are used for analysis as the area function is well calibrated in this range and the substrate effect is negligible (indentation depth is $<10\%$ of film thickness).⁵²

In the scratch tests, the Berkovich tip is slid at a speed of $0.625 \text{ \mu m s}^{-1}$ over the surface of the film while applying a compressive load of 500 μN . The tip is aligned in the edge-forward orientation.⁵³ The length of each scratch line is 10 \mu m . For each sample, 2 different locations and 5 scratches with a spacing of 10 \mu m are made on each location. The normal displacement and lateral force are recorded throughout the scratch test.

The fracture toughness of the films is characterized using a nanoindentation-based pillar-splitting method.^{24,54} The micropillars are fabricated using a FIB (FEI Strata DB235) with a 30 kV gallium ion beam. All micropillars are fabricated by first milling cylinders at a 500 pA current, followed by milling finer concentric cylinders at lower currents (300 pA and 100 pA). The pillar diameters range from 1.5 to 2.7 μm and have aspect ratios (pillar height/pillar diameter) greater than 1 to relax any possible residual stress on the upper portion of the pillar.⁵⁴ For each sample, at least five micropillars are milled and SEM images are taken after the FIB milling to measure the radii of the micropillars. Then, the samples are tested with a Berkovich indenter under load control. For each pillar, the indenter is first raster scanned around the pillar to locate the center and it is indented at the center at a loading rate of 200 $\mu\text{N/s}$ until a critical load is reached. This critical load is identified by a jump in displacement in the force-displacement curve. The fracture toughness, K_{IC} , is calculated as⁵⁴

$$K_{IC} = \gamma \frac{P_c}{R^{3/2}} \quad (1)$$

where P_c is the critical load, R is the radius of the pillar and γ is a dimensionless coefficient calculated as follows:²⁴

$$\gamma = \frac{\alpha}{0.1859} \sqrt{\frac{E}{H}} \quad (2)$$

Here, E and H are the elastic modulus and hardness of the films and α is a geometric parameter (0.016 for Berkovich tip). After nanoindentation, the micropillars are imaged using SEM. If the tip is not well aligned near the center of the pillar or the pillars detached from the Si wafer, the data from the test is excluded. The fracture toughness reported for each sample is the average of at least 4 pillars.

3. Results and Discussion

In this work, we use capillary rise infiltration (CaRI) to generate nanocomposite films with high volume fraction of nanoplatelets (NPTs). As shown in Figure 1, we use flow coating to assemble gibbsite NPTs into a densely packed, highly aligned structure atop of a polystyrene (PS) film. Subsequently, the bilayer film is annealed above the T_g of PS to induce infiltration into the NPT packing and generate a polymer-infiltrated NPT film.

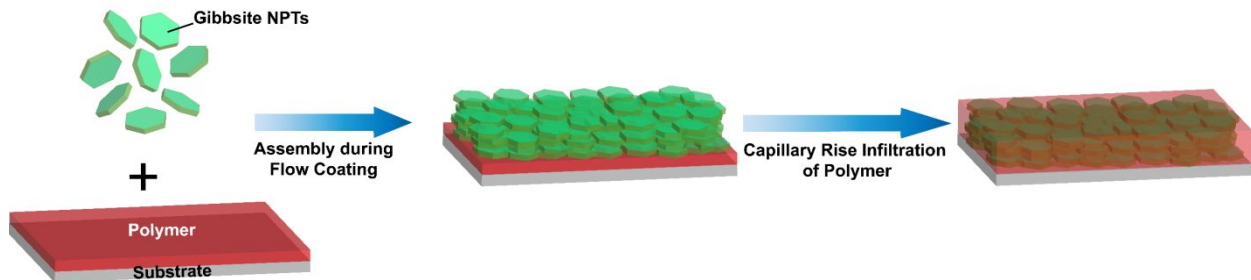


Figure 1. Schematic illustration showing the process of fabricating a polymer-infiltrated NPT film by assembly of gibbsite NPTs and capillary rise infiltration (CaRI) of polymer into the NPT packing.

3.1 Flow coating of gibbsite NPTs

Gibbsite NPTs with a well-defined hexagonal shape are synthesized using a hydrothermal method.⁴⁸ The diameter of NPTs is 213 ± 22 nm based on SEM images (Figure S1) and the thickness of the NPTs is 8.2 ± 2.3 nm determined from AFM measurement (Figure S2). Figure S3 shows the XRD pattern of the NPTs which agrees with monoclinic gibbsite (JCPDS 74-1775).⁴⁸ The synthesized NPTs have a high AR (~ 26) and their diameter and thickness can be further increased to 465 ± 64 and 18 ± 5 nm, respectively, using a seeded-growth method (Figure S1-2).

As illustrated in Figure 2, we use flow coating to assemble gibbsite NPTs. A gibbsite NPT suspension made of 8 wt% of NPTs in a mixture of water and ethanol is initially confined between a glass blade and a substrate by capillarity. A liquid film is then drawn out of the suspension by moving the substrate at a given speed. During solvent evaporation, gibbsite NPTs rapidly self-orient parallel to the substrate, aided by the strong electrostatic repulsion and isotropic-to-nematic transition template by the two interfaces.⁵⁵ When solvent completely evaporates, a dense solid film is formed with NPTs in a face-to-face stacked state. Figure 2(c) and (d) show the cross-sectional and top-down SEM images of the flow-coated gibbsite NPT films which confirm that NPTs are densely packed and aligned parallel to the substrate in an overlapping rearrangement, similar to discotic-nematic structure.⁵⁶ No observable aggregates can be seen in the SEM images and across the entire coating (Figure S4(f)). High uniformity of the film is maintained as thickness increases or as coating area increases (Figure S4(e-f)). In contrast, spin coating, which is a widely used technique to prepare nanoparticle films, results in non-uniform films with poor alignment and aggregates (Figure S5).

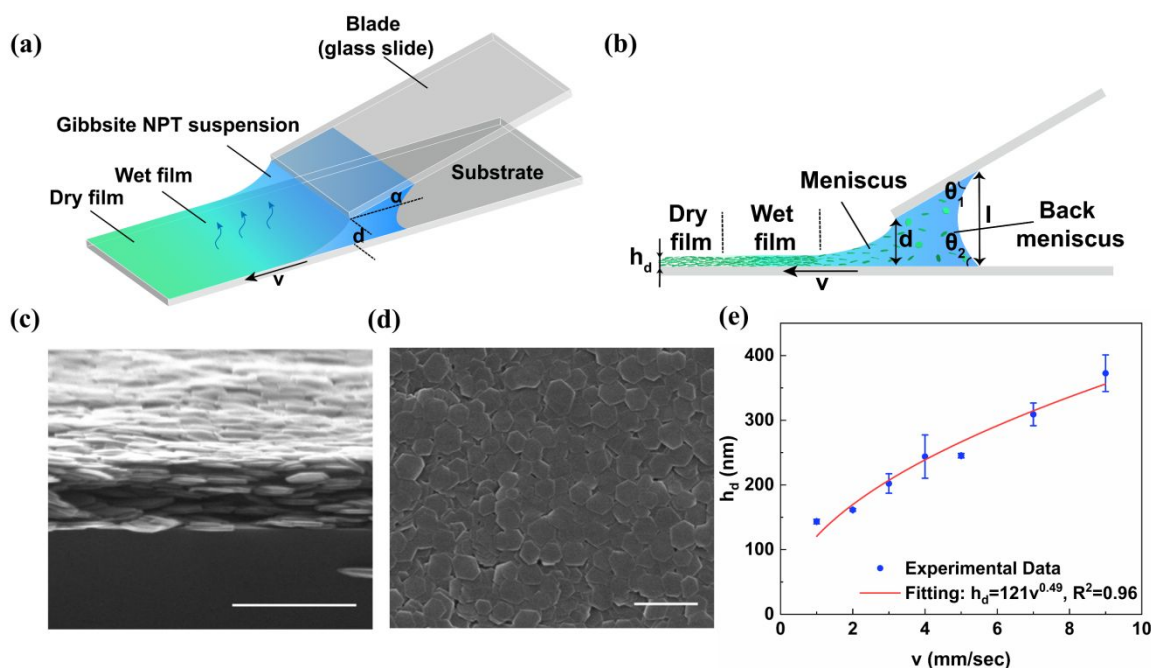


Figure 2. Schematic of the (a) perspective and (b) side view of flowing coating of gibbsite NPT suspension. (c) Cross-sectional and (d) top-down SEM image of a gibbsite NPT film deposited on a Si wafer. All scale bars are 500 nm. (e) Dry film thickness h_d as a function of substrate velocity v . These films are deposited using a blade at an angle of 25° and a gap height of $60 \mu\text{m}$ with $6 \mu\text{l}$ of an 8 wt% gibbsite NPT suspension. Red solid line is a power law fit to the data.

Addition of ethanol into gibbsite aqueous suspensions is found to be essential for generating uniform films via flow coating. Zeta-potential (ζ) of the purified gibbsite NPTs in deionized water is 32.8 ± 1.0 mV, keeping gibbsite stable in solution in both the aqueous and the alcoholic dispersions. The addition of ethanol lowers the surface tension of the solvent and prevents the dewetting of receding meniscus from the substrate, especially when coated on a polymer film, during flow coating. More importantly, ethanol accelerates solvent evaporation and ensures that the wet film dries at a uniform velocity along the width (supporting video 1). Without addition of ethanol, the alignment of NPTs is not significantly affected; however, the wet film dries slowly and thus results in a non-uniform film with thin edges and a thick center (Figure S4(b-d)).

The thickness of films deposited by flow coating depends on multiple factors including blade angle (Figure S4(h)), gap height, suspension/solution concentration and substrate velocity.⁴⁷ Here, when the blade angle, gap height and suspension concentration are held constant, the dry film thickness (h_d) increases with the substrate velocity (v) (Figure 2(e)). This trend agrees well with the Landau-Levich regime where the substrate velocity is high and the amount of solvent dragged by the substrate is larger than the amount of evaporated solvent. As substrate velocity increases, the friction drag pulls out a thicker wet film and leads to a thicker dry film.^{47,57} It can also be seen that h_d shows a power-law dependence on v ($h_d \sim v^{0.49}$). The power-law exponent (0.49) is lower than the value predicted for Landau-Levich regime (0.67),⁵⁷ which may be attributed to the shear thinning effect of gibbsite suspensions.⁵⁸ A previous study has shown that the exponent can be smaller than 0.67 for shear-thinning suspensions.⁵⁹

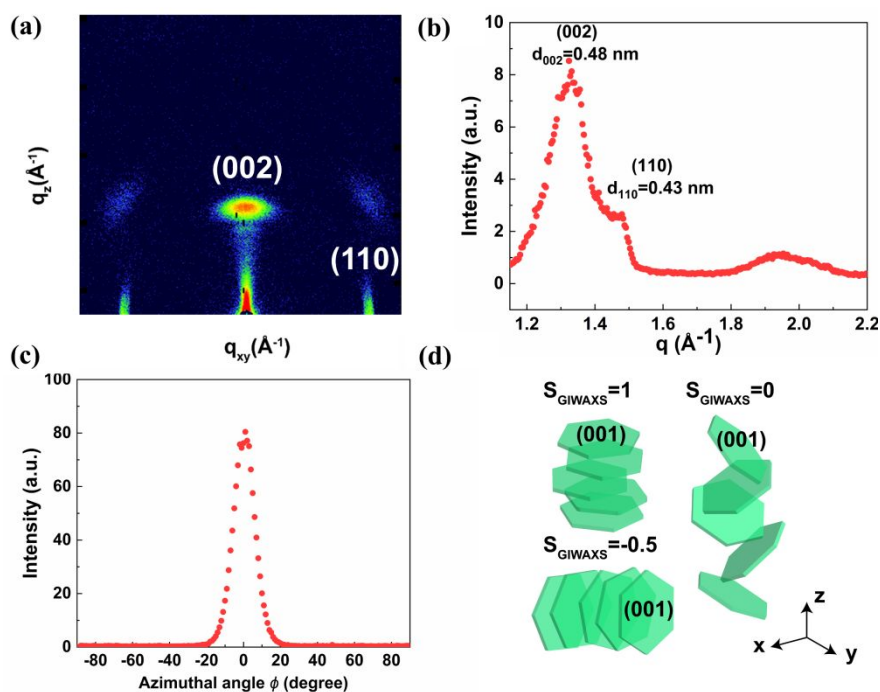


Figure 3. (a) Two-dimensional (2D) GIWAXS pattern of a ~ 200 nm flow-coated gibbsite NPT film. One-dimensional (1D) (b) radial intensity profile constructed from (a) and (c) azimuthal intensity profile across the (002) peak. (d) Schematics of NPT alignments corresponding to different S_{GIWAXS} .

GIWAXS measurements are performed to quantify the alignment of gibbsite NPTs in the flow-coated films. Figure 3(a) and (b) shows a typical 2D GIWAXS pattern and its corresponding 1D radial intensity profile. The scattering vector q can be decomposed to q_z and q_{xy} , where q_z is defined as the q component perpendicular to the substrate and q_{xy} is defined as the q component parallel to the substrate. q_x and q_y are expected to be the same because the film is isotropic in the x-y plane which can be confirmed by ellipsometry and will be discussed later. The scattering pattern shows strong anisotropy with sharp features near $q_z = 1.30 \text{ \AA}^{-1}$ and $q_{xy} = q_z = 1.48 \text{ \AA}^{-1}$. These peaks correspond to d-spacing values of two lattice planes: $d_{(002)} = 0.48 \text{ nm}$ and $d_{(110)} = 0.43 \text{ nm}$ of gibbsite NPTs.⁶⁰ The azimuthal analysis of the primary (002) peak allows us to quantify the alignment of gibbsite NPTs. After background subtraction, GIWAXS-derived Herman's order parameter is calculated based on the scattering near $q = 1.3 \text{ \AA}^{-1}$ using:⁶¹

$$S_{GIWAXS} = \frac{\langle 3\langle \cos^2 \phi \rangle - 1 \rangle}{2} \quad (3)$$

$$\langle \cos^2 \phi \rangle = \frac{\int_0^{90} I(\phi)(\cos^2 \phi)(\sin \phi) d\phi}{\int_0^{90} I(\phi)(\sin \phi) d\phi} \quad (4)$$

where ϕ is the azimuthal angle in the reciprocal space with $\phi = 0^\circ$ defined along q_z , $I(\phi)$ is the angle dependent scattering density. S_{GIWAXS} can vary between -0.5 and 1. S_{GIWAXS} close to 1 would correspond to a sharp peak along q_z (as shown in Figure 3(a)) and indicate a strong tendency of (001) lattice planes to stack parallel to the substrate (Figure 3(d)). $S_{GIWAXS} = -0.5$ would correspond to a sharp peak along q_{xy} and the preferential orientation of (001) planes perpendicular to the substrate, whereas $S_{GIWAXS} = 0$ represents no preferential (isotropic) orientation. The S_{GIWAXS} for the flow-coated sample is 0.96, suggesting that NPTs are very well aligned with surfaces facing the substrate, consistent with SEM images (Figure 2(c)). We also confirm that the high degree of alignment can be achieved for larger NPT (Diameter = $465 \pm 64 \text{ nm}$) packings (Figure S6, $S_{GIWAXS} = 0.95$).

3.2 Capillary rise infiltration of polymer into gibbsite NPT films

Gibbsite NPTs with AR>20 pack very densely in the flow-coated films due to the high degree of alignment. It is not clear if there are interconnected pores in these dense films that would enable infiltration of polymer via CaRI. To investigate the possibility of polymer infiltration into the packings, we use spectroscopic ellipsometry to measure the optical properties and thickness changes of the films.

Ellipsometry modeling of a ~300 nm thick neat gibbsite NPT film made via flow coating from an 8 wt% suspension is shown in Figure S7 and Table S1. A uniaxial model, where two Cauchy dispersion relations are used to describe refractive index for the in-plane (n_o) and out-of-plane (n_e) directions of the film, can describe the data with high accuracy. The birefringence of gibbsite NPT films, defined as $\Delta n = n_e - n_o$,⁴³ is used to calculate the packing fraction of gibbsite NPTs (see Supporting Information for a more detailed description).⁴³ By averaging measurements on 40 films, the birefringence of NPT films is determined to be 0.06, corresponding to a packing fraction of 0.84. This is significantly higher than the random close packing of spherical NPs (0.64). The packing fraction and birefringence of NPT films can also be varied by changing platelet size (see Supporting Information).

By flow coating NPTs on a spin-coated PS layer ($M_n = 8,000 \text{ g mol}^{-1}$), a bilayer film is formed and subsequently subjected to a heat treatment. We note that while the T_g of bulk PS 8k is around 367 K, an increase in the T_g of PS 8k undergoing CaRI has been observed due to physical confinement effect.^{29,30} Thus, higher temperatures are used to overcome this effect and accelerate the CaRI process. Figure S9 shows typical *in situ* ellipsometry raw data (amplitude ratio (ψ) and phase shift (Δ)) of such a bilayer film annealed at 403 K and Table 1 summarizes the fitting result of the data with a two-layer Cauchy model. Both ψ and Δ undergo significant changes during annealing, indicating substantial changes in the structure of the bilayer. The significant increase in the refractive index of NPT layer as well as decrease in thickness of PS layer confirm that PS can indeed infiltrate into NPT packings. Based on the thickness change of PS layer, the volume fraction of PS in the NPT/PS composite film is calculated to be 0.19 ($\phi_{PS} = \Delta h_{PS}/h_{NPT}$), close to the estimation based on the birefringence. The birefringence of the NPT film turns positive upon full infiltration, in agreement with theoretical predictions (Figure S8(b)).

To study the dynamics of polymer infiltration, gibbsite NPT/PS-8k bilayer films with different NPT layer thickness are annealed at 423 K and monitored using *in situ* ellipsometry. When there is no further increase in the refractive index of NPT layer or decrease in the thickness of PS layer, infiltration of polymer is completed, and thus the time required to form gibbsite/PS-8k composite can be determined. Figure 4 shows the linear dependence of composite layer thickness squared, l_{comp}^2 on time, t , for the gibbsite NPT/PS-8k system, consistent with previous CaRI systems that followed the Lucas–Washburn model:^{20,21,29,30}

$$l^2 = \frac{\sigma R \cos \theta}{4\tau^2 \mu} t \quad (7)$$

where l is the height of the NPT layer infiltrated by the polymer, σ is the surface tension of the polymer melt, R is the mean pore radius in the NPT packing, θ is the contact angle of the polymer melt on the NPT surface, τ is the tortuosity of packaging, μ is the viscosity of the polymer melt, and t is the annealing time. Based on slope of l_{comp}^2 vs t and using the literature values for other parameters in the Lucas-Washburn prefactor, the tortuosity τ of NPT is estimated to be >26 (see Supporting Information for a more detailed description). Tortuosity is known to be a function of porosity, particle dimension and orientation.⁶² Since the gibbsite NPT packing has a porosity less than 20 vol% and is composed of well-aligned high AR NPTs in an overlapping rearrangement,

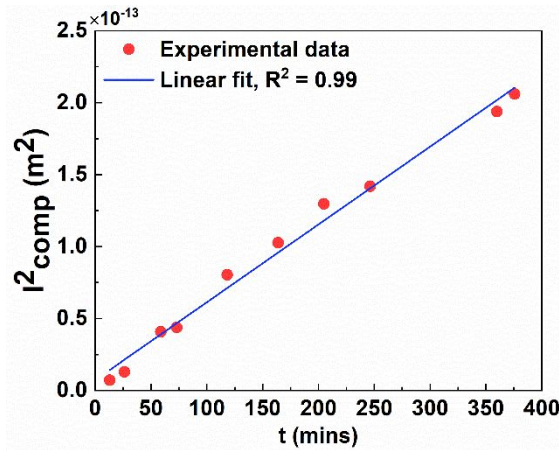


Figure 4. The composite layer thickness squared, l_{comp}^2 of gibbsite NPT/PS-8k composite as a function of time, t , when gibbsite NPT/PS-8k bilayer films are annealed at 423 K. The blue line shows a linear fit and agrees well with the Lucas-Washburn equation.

the tortuosity is significantly increased compared to spherical NP packings ($\tau = 1.95$). Such a high tortuosity suggests that polymer-infiltrated NPT packings would make an ideal gas barrier.⁶³

Table 1 Thickness, refractive index, and polymer volume fraction for complete infiltration of a gibbsite NPT/PS-8k bilayer film annealed at 403 K

		Gibbsite NPT/PS-8k bilayer	
		Before annealing	After annealing
Thickness (nm)	NPT layer	272.12	
	PS layer	242.85	190.69
Refractive index of NPT layer@ 632.8 nm	n_o	1.472	1.564
	n_e	1.432	1.580
ϕ_{PS}		0.19	

Polymer infiltration is also confirmed by SEM images and UV-vis spectra of gibbsite NPT/PS films. Figure 5 shows the cross-sectional SEM images of a gibbsite NPT ($\sim 1.7 \mu\text{m}$)/PS-8k ($\sim 500 \text{ nm}$) bilayer film before and after thermal annealing at 453 K. The outlines of NPTs can be clearly identified before annealing. In comparison, after annealing, the NPTs are surrounded by PS. The thickness of NPT layer remains unchanged while the thickness of PS layer decreases due to infiltration. The volume fraction of PS in the composite layer (0.17) by calculating the decrease in the PS layer thickness agrees well with the porosity determined by ellipsometry. Due to the matching of the refractive index between PS (1.588@ 632.8 nm) and gibbsite NPTs (1.568-1.587)⁶⁴, such polymer-infiltrated NPT film becomes highly transparent with $>80\%$ transmittance over the entire visible range (Figure S10).

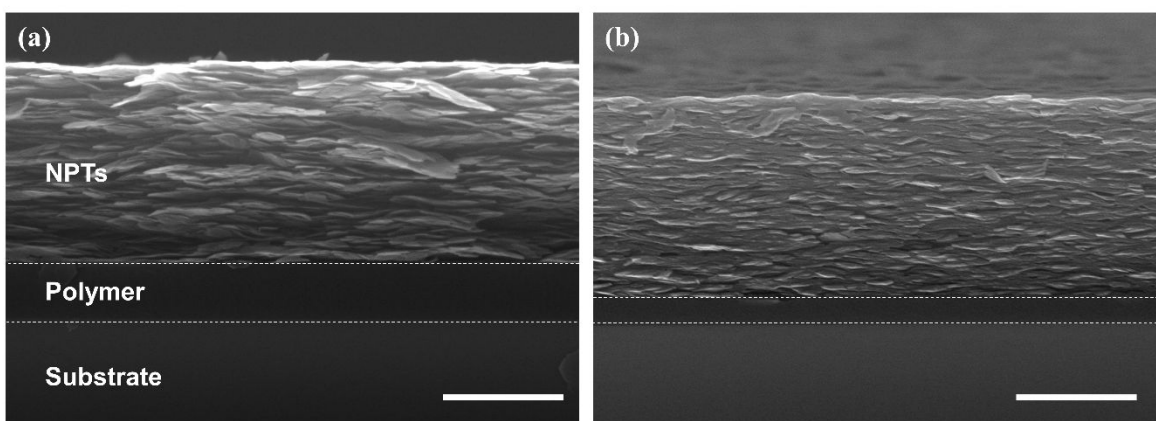


Figure 5. Cross-sectional SEM images of a bilayer film composed of a gibbsite NPT layer atop a PS ($M_n = 8\,000 \text{ g mol}^{-1}$) layer (a) before infiltration and (b) after infiltration. All scale bars are $1 \mu\text{m}$.

3.3 Mechanical properties of gibbsite/PS PINFs

The mechanical properties of gibbsite NPT packings before and after PS infiltration are characterized to study the effect of polymer infiltration via CaRI on mechanical properties. Furthermore, we compare the mechanical properties of the NPT films with the previously reported properties of TiO₂ NP packings to understand the effect of particle shape and packing. The modulus and hardness of gibbsite NPT (>2 μ m)/PS bilayer films before and after CaRI are characterized using quasi-static nanoindentation with a Berkovich tip. The thickness of PS layer is controlled to be slightly thicker than what would be necessary to fully saturate the NPT layer (i.e. \sim 20% of NPT thickness). The reduced Young's modulus is extracted from the unloading curves using the Oliver and Pharr method,⁵¹ although the film has an anisotropic structure. As shown in Figure 6(a), the modulus and hardness of neat NPT packings are 6.59 ± 0.77 GPa and 0.23 ± 0.06 GPa, respectively. Lower modulus and hardness are observed in the packings of larger NPTs which have a lower packing fraction (0.72, Table S4). These values are lower than packings of TiO₂ nanoparticles with major axes of 37.4 ± 6.7 nm and minor axes of 28.8 ± 4.1 nm ($E=12.9 \pm 0.5$ GPa, $H=0.27 \pm 0.02$ GPa).²¹ The modulus of NP packing is related to the pore structure, porosity, packing geometry, NP bonding and the elastic modulus of the NPs.⁶⁵ Although the gibbsite NPT films have lower porosity (<0.2) than TiO₂ NP packings (0.45), the modulus of NPT packings is lower than that of TiO₂ NP packings, which we believe is due to the significantly lower elastic modulus of gibbsite (49 ± 2 GPa)⁶⁶ compared to that of anatase TiO₂ (178 ± 1 GPa).⁶⁷ SEM observation of indented gibbsite NPT packings show that NPTs themselves are deformed and, in some cases, fracture during indentation (Figure S11), whereas TiO₂ NPs do not plastically deform but rather undergo rearrangements during indentation. The reduced Young's modulus and hardness of NPT films after polymer infiltration increase to 25.45 ± 2.85 GPa and 1.58 ± 0.27 GPa, respectively. The enhancement of modulus and hardness after polymer infiltration is much more significant in

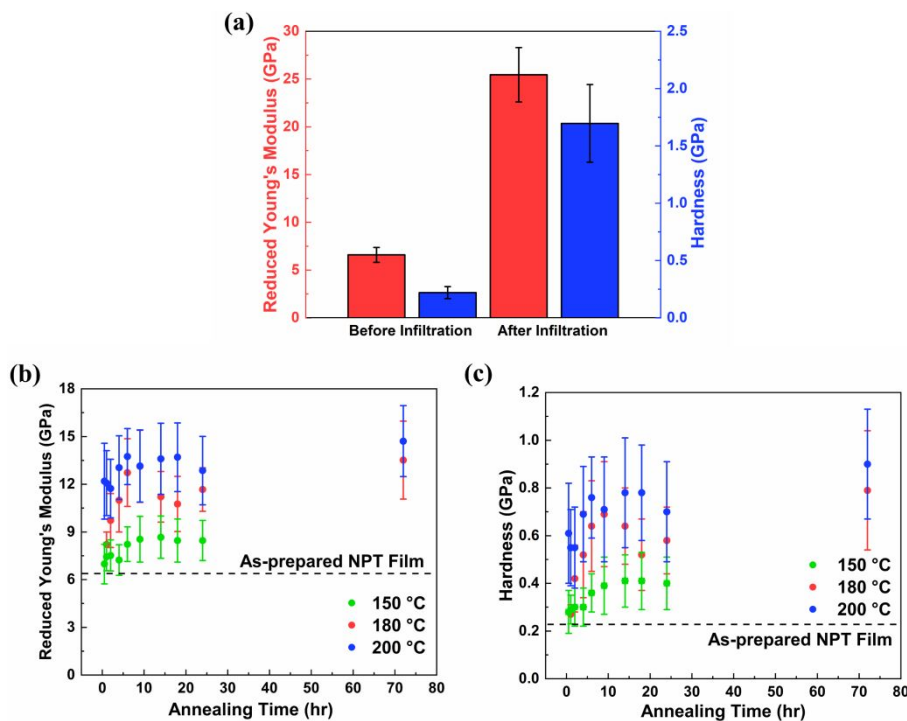


Figure 6. (a) Reduced Young's modulus and hardness of neat NPT films and polymer-infiltrated NPT films. (b) Reduced Young's modulus and (c) hardness of neat NPTs films as a function of annealing time at 150 °C, 180 °C and 200 °C.

NPT packings (3.9 times in *E* and 6.9 times in *H*) than in TiO₂ NP packings (2.5 times in *E* and 3.5 times in *H*). These values are also superior to the moduli and hardnesses of the recently reported nacre-like films including graphene oxide/poly (vinyl alcohol) (RGO/PVA),⁶⁸ graphene oxide/cross-linking agent (GO/CA)⁶⁹ and glass flake/PMMA composites.⁷⁰

To further investigate the origin of the observed stiffening and hardening effects upon CaRI, neat gibbsite NPT films are heat-treated at 150, 180 and 200 °C. Surprisingly, neat NPT films show appreciable temperature- and time-dependent stiffening and hardening effects as shown in Figure 6(b-c). The modulus and hardness of neat NPT film after annealing at 180 °C for 24 hrs is 1.8 and 2.5 times those of the as-prepared films, respectively. In-situ ellipsometry studies of gibbsite NPT film at 200 °C and 400 °C indicate that gibbsite NPTs are relatively stable at 200 °C and that they undergo phase transform only at higher temperature (~230 °C, see Supporting Information for a more detailed description). Thus, it is unlikely that the stiffening and hardening effects observed at $T \leq 200$ °C result from phase transformation of gibbsite. Rather, since the surface of gibbsite NPTs have abundant -OH groups,⁷¹ the stiffening and hardening may be due to thermally promoted surface dehydroxylation and formation of Al-O-Al bridges between adjacent surface Al-OH groups. Forming of oxide bridges have been reported in prior studies that probed the mechanical properties of heat-treated alumina-coated silica NPs,⁷² stöber silica NPs⁷³ and silica surfaces.⁷⁴ TiO₂ NP films also exhibit stiffening and hardening effects when heated to 180 °C (Table S3); however, the changes are relatively less significant. The contact area between NPTs in well-aligned NPT films are significantly larger than that in packings of AR1 NPs, facilitating the formation of oxide bridges between NPTs. Thus, the large stiffening and hardening effects observed in annealed bilayers originate from the formation of oxide bridges and the infiltration of polymer, both of which strengthen the bonding between NPTs.

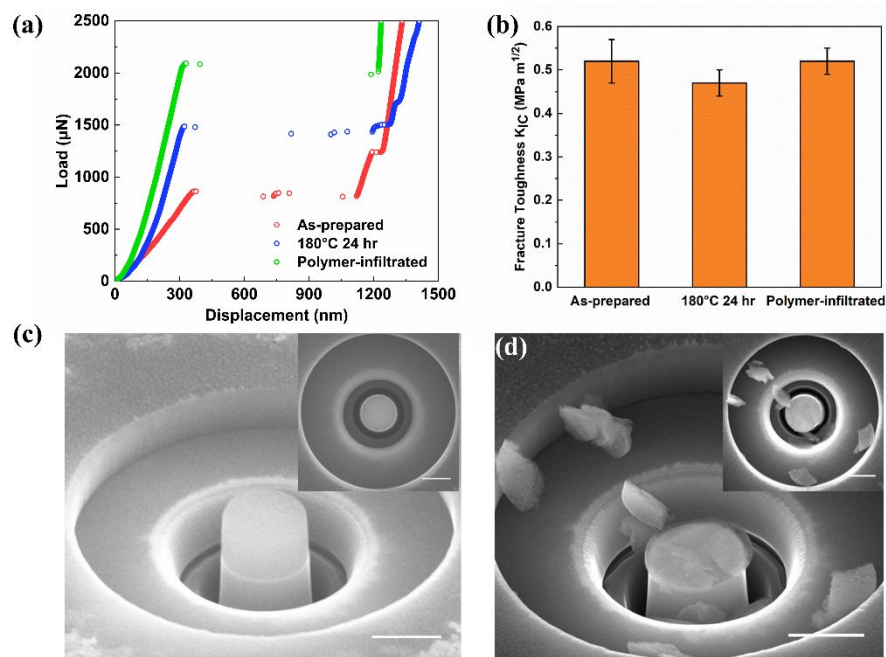


Figure 7. (a) Example load-displacement curves from pillar-splitting tests on as-prepared, heat-treated (180°C for 24 hrs) and polymer-infiltrated NPT films. (b) Fracture toughness of NPT films. SEM images of a FIB-milled micropillar on a heat-treated neat NPT film (c) before and (d) after pillar-splitting fracture test. Images are acquired at a tilt angle of 40°. The insets are corresponding top-down SEM images. All scale bars are 2 μm.

The fracture toughness of NPT films is measured with a nanoindentation-based pillar-splitting method. This method provides several advantages including: (1) simplicity of sample preparation and testing, (2) minimizing the influence of FIB damage and film residual stress on measurements, and (3) no required post-test measurements of crack length.⁵⁴ Representative load-displacement curves from the pillar splitting tests of as-prepared, heat-treated and polymer-infiltrated gibbsite NPTs are shown in Figure 7(a). Each curve shows an initial elastic-plastic response until a jump in displacement that corresponds to unstable crack propagation at a critical load P_c . Additional kinks can also be seen in the force-displacement curves for some pillars (e.g. red and blue curves in Figure 7(a)), indicating secondary unstable crack propagation events as the tip is indented further into the pillars. In contrast to previously studied TiO₂ NP film where there is a large load drop after crack propagation, the load drop in NPT films is quite small (<100 μN), indicating increased plasticity.²⁴ The fracture toughness of as-prepared gibbsite NPT films reaches 0.52 ± 0.05 MPa \cdot m^{1/2}, which is over 7 times that of AR1 TiO₂ NP films ($K_{Ic}=0.07$ MPa \cdot m^{1/2}).²⁴ This value is also higher than fracture toughness of random packings of TiO₂ ellipsoids (AR=4),⁷⁵ packings of silica nanospheres⁷⁶ and NP packings treated with atomic layer deposition.^{77,78} This comparison clearly demonstrates the advantage of the aligned nanostructure that has been attributed to high fracture toughness of various composite materials. To propagate cracks along the loading direction, cracks have to either propagate through the NPTs (platelet fracture, see supporting Figure S11) or deflect around the NPTs and pull them out.⁷⁹ Both mechanisms result in greater energy dissipation for crack propagation than is necessary to propagate a crack through low AR NP packings.

SEM images of the micropillars after indentation are taken to confirm splitting of the pillars and observe the crack type. As-prepared, heat-treated and polymer-infiltrated NPT films all show

similar fracture patterns. As shown in Figure 7(c-d), the fractured pieces of indented pillars are found on the outer circular trench that is milled to allow ample space for the pillar to deform during nanoindentation. Only a small part of the pillar remains on the substrate. A close look at the fractured pieces indicates a 3-way splitting, where cracks propagated from the corner of the indenter to the edge of the pillar due to stress concentration. More than three fractured pieces can be found for the pillar in Figure 7(d) possibly due to the propagation of secondary crack. The remaining part of the pillar shows large residual imprint matching the shape of the indenter which can be better observed for an indented pillar where the fractured debris do not fully separate (Figure S13). This type of crack indicates significant plasticity in NPT films.^{24,54,80}

Interestingly, heat-treated and polymer-infiltrated NPT films both have a fracture toughness of $\sim 0.5 \text{ MPa m}^{1/2}$ which is similar to that of the neat NPT films. This lack of significant change in the fracture toughness with infiltration is different than what was observed for polymer-infiltrated TiO_2 NP packings.²⁴ We believe high packing fraction of NPTs and more importantly high alignment of NPTs make it difficult for polymer to infiltrate where the flat faces of NPTs are in direct contact with each other.³⁹ In this case, fracture energy cannot be dissipated efficiently by diverting cracks to follow a tortuous path and allowing platelet sliding. Thus, cracks propagate through the NPTs which we observe under SEM.

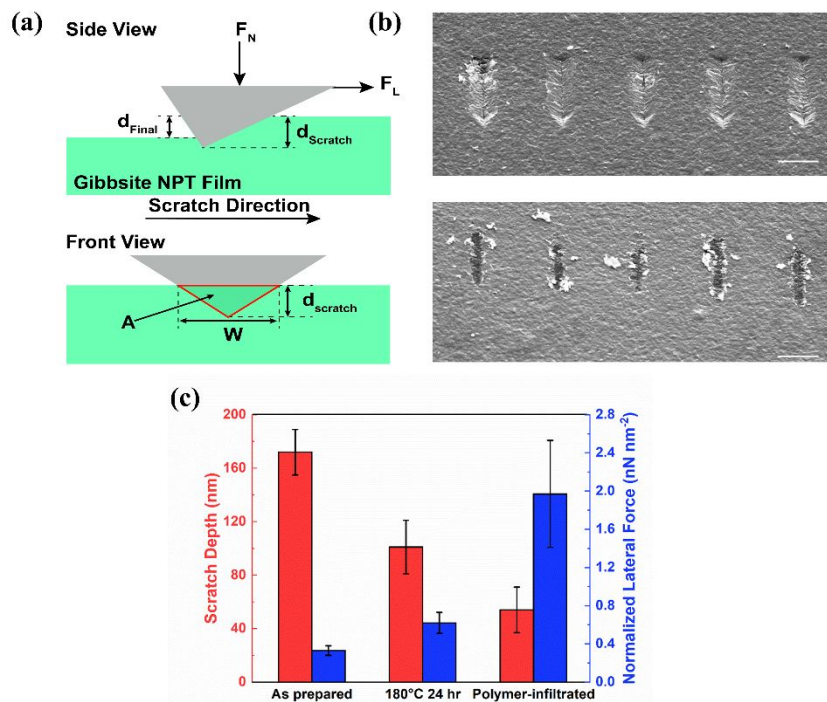


Figure 8. (a) Schematic of the scratch test set-up. (b) SEM images of the resulting grooves on as-prepared NPT film (top) and polymer-infiltrated NPT film (bottom) after scratch tests. All scale bars are 5 μm . (c) Final scratch depth and normalized lateral force of as-prepared, heat-treated (180 °C 24 hr) and polymer-infiltrated gibbsite NPT films.

The high hardness of polymer-infiltrated NPT films could make them useful in applications requiring wear and scratch resistance. We evaluate their scratch resistance by performing constant load scratch tests using a Berkovich tip in an edge-forward orientation (Figure 8(a)). The normal load and lateral displacement for the scratch test setup is shown in Figure S14. As observed in the SEM images of the scratched surfaces (Figure 8(b)), microcracking/chipping are observed in both

films; polymer-infiltrated NPT films show much narrower grooves compared to un-infiltrated films. Figure 8(c) shows the final scratch depth obtained by rescanning the surface with the same tip after each scratch. The scratch depth of NPT films decreases from 172 ± 17 nm to 101 ± 20 nm when the NPT is heat treated at 180 °C and further decreases to 54 ± 17 nm after polymer infiltration, indicating enhanced scratch resistance due to oxide bridge formation and polymer infiltration. Another parameter we use to quantify the scratch resistance is the lateral force divided by the cross-sectional area of the grooved track, which is a measure of the stress required to deform and remove materials during scratch. As shown in Figure 8(c), the normalized lateral force increases by 6 times in NPT films after polymer infiltration. The extent of scratch improvements observed in polymer-infiltrated NPT films is greater than that observed for polymer-infiltrated TiO_2 NP packings (Figure S15). The large enhancement of scratch resistance in NPTs is consistent with the modulus and hardness increase we observe in nanoindentation tests. We emphasize that although neat NPT films are relatively weak, soft, and scratch-prone, polymer-infiltration significantly enhances their mechanical properties, by reinforcing the interactions between the well-aligned NPTs.

4. Conclusions

In summary, we demonstrate a facile and scalable process to fabricate PINFs with highly aligned NPTs by combining flow coating and CaRI. The flow coating process allows for the fabrication of uniform gibbsite NPT assemblies over large areas. The resulting NPT packings consist of well-aligned NPTs with extremely high packing fraction (>80 vol%). By annealing NPT/polymer bilayer films above the glass transition temperature of the polymer, polymer is induced to infiltrate into the interstices of the NPT packing through capillarity, producing PINFs with a brick-and-mortar structure. By performing detailed nanoindentation and nanoscratch tests, we find the modulus, hardness and scratch resistance of PINFs are 3.9, 6.9 and 6.0 times those of neat NPT films, respectively. The significant enhancement in mechanical properties after polymer infiltration is attributed to the Al-O-Al bond formation and polymer filling the interstices, both strengthening the interactions between NPTs. Our results demonstrate the benefits of producing nanocomposite films with a high concentration of well aligned NPTs. A topic for a future study is to tune the alignment of the NPTs through different processing routes and explore the correlation between the alignment of the NPTs and the mechanical properties of the films. In addition, while our study uses gibbsite NPTs as a model anisotropic nanomaterial, other types of anisotropic nanomaterials can be processed into thin films with different degrees of alignment enabling other applications in solid lubrication and barrier coatings. In particular, the high tortuosity in the PINFs makes it an ideal candidate for gas barrier applications. Understanding of the effect of particle shape, particle alignment and polymer type on the gas barrier properties of PINFs will be the focus of future investigations.

Reference

- 1 V. R. Dugyala, S. V. Daware and M. G. Basavaraj, *Soft Matter*, 2013, **9**, 6711–6725.
- 2 L. Yang, Z. Zhou, J. Song and X. Chen, *Chem. Soc. Rev.*, 2019, **48**, 5140–5176.
- 3 O. Erdem, S. Foroutan, N. Gheshlaghi, B. Guzelturk, Y. Altintas and H. V. Demir, *Nano Lett.*, 2020, **20**, 6459–6465.

- 4 J. D. Forster, J. G. Park, M. Mittal, H. Noh, C. F. Schreck, C. S. O'Hern, H. Cao, E. M. Furst and E. R. Dufresne, *ACS Nano*, 2011, **5**, 6695–6700.
- 5 J. Kim, J. Peretti, K. Lahlil, J. P. Boilot and T. Gacoin, *Adv. Mater.*, 2013, **25**, 3295–3300.
- 6 R. A. Alvarez-Puebla, E. R. Zubarev, N. A. Kotov and L. M. Liz-Marzán, *Nano Today*, 2012, **7**, 6–9.
- 7 J. B. Rivest, S. L. Swisher, L. K. Fong, H. Zheng and A. Paul Alivisatos, *ACS Nano*, 2011, **5**, 3811–3816.
- 8 K. Deng, Z. Luo, L. Tan and Z. Quan, *Chem. Soc. Rev.*, 2020, **49**, 6002–6038.
- 9 K. Thorkelsson, P. Bai and T. Xu, *Nano Today*, 2015, **10**, 48–66.
- 10 C. Harito, D. V Bavykin, B. Yulianto, H. K. Dipojono and F. C. Walsh, *Nanoscale*, 2019, **11**, 4653.
- 11 M. Boota, B. Anasori, C. Voigt, M.-Q. Zhao, M. W. Barsoum and Y. Gogotsi, *Adv. Mater.*, 2016, **28**, 1517–1522.
- 12 H. Tang, J. Wang, H. Yin, H. Zhao, D. Wang and Z. Tang, *Adv. Mater.*, 2015, **27**, 1117–1123.
- 13 Z. Wang, Y. Fu, W. Meng and C. Zhi, *Nanoscale Res. Lett.*, 2014, **9**, 1–7.
- 14 X. Huang, C. Zhi and P. Jiang, *J. Phys. Chem. C*, 2012, **116**, 23812–23820.
- 15 X. Ye, S. G. Kandlikar and C. Li, *Eur. Phys. J. E*, 2019, **42**, 1–34.
- 16 S. Gupta, Q. Zhang, T. Emrick and T. P. Russell, *Nano Lett.*, 2006, **6**, 2066–2069.
- 17 Z. Wang, K. Rolle, T. Schilling, P. Hummel, A. Philipp, B. A. F. Kopera, A. M. Lechner, M. Retsch, J. Breu and G. Fytas, *Angew. Chemie*, 2020, **132**, 1302–1310.
- 18 Y. F. Huang, Z. G. Wang, H. M. Yin, J. Z. Xu, Y. Chen, J. Lei, L. Zhu, F. Gong and Z. M. Li, *ACS Appl. Nano Mater.*, 2018, **1**, 3312–3320.
- 19 R. Hoffmann, V. Baric, H. Naatz, S. O. Schopf and A. Hartwig, *ACS Appl. Nano Mater.*, 2019, **2**, 2273–2282.
- 20 Y. R. Huang, Y. Jiang, J. L. Hor, R. Gupta, L. Zhang, K. J. Stebe, G. Feng, K. T. Turner and D. Lee, *Nanoscale*, 2015, **7**, 798–805.
- 21 J. L. Hor, Y. Jiang, D. J. Ring, R. A. Riggelman, K. T. Turner and D. Lee, *ACS Nano*, 2017, **11**, 3229–3236.
- 22 N. Manohar, K. J. Stebe and D. Lee, *ACS Macro Lett.*, 2017, **6**, 1104–1108.
- 23 R. B. Venkatesh, S. H. Han and D. Lee, *Nanoscale Horizons*, 2019, **4**, 933–939.
- 24 Y. Jiang, J. L. Hor, D. Lee and K. T. Turner, *ACS Appl. Mater. Interfaces*, 2018, **10**, 44011–44017.
- 25 B. F. Donovan, R. J. Warzoha, R. B. Venkatesh, N. T. Vu, J. Wallen and D. Lee, *ACS Appl. Nano Mater.*, 2019, **2**, 6662–6669.
- 26 X. Zeng, S. Xu, P. Pi, J. Cheng, L. Wang, S. Wang and X. Wen, *J. Mater. Sci.*, 2018, **53**, 10554–10568.
- 27 X. Zeng, K. Yang, K. Yang, S. Xu, M. Xu, P. Pi and X. Wen, *Mater. Res. Express*, 2019, **6**, 085025.
- 28 J. Zhang and L. Zhang, *ACS Appl. Nano Mater.*, 2019, **2**, 6368–6377.
- 29 J. L. Hor, H. Wang, Z. Fakhraai and D. Lee, *Soft Matter*, 2018, **14**, 2438–2446.
- 30 J. L. Hor, H. Wang, Z. Fakhraai and D. Lee, *Macromolecules*, 2018, **51**, 5069–5078.
- 31 T. Liu, B. Chen and J. R. G. Evans, *Bioinspiration and Biomimetics*, 2008, **3**, 016005.
- 32 J. Sun and B. Bhushan, *RSC Adv.*, 2012, **2**, 7617–7632.
- 33 H. Zhao, Z. Yang and L. Guo, *NPG Asia Mater.*, 2018, **10**, 1–22.
- 34 U. G. K. Wegst, H. Bai, E. Saiz, A. P. Tomsia and R. O. Ritchie, *Nat. Mater.*, 2015, **14**,

- 23–36.
- 35 J. Wang, Q. Cheng and Z. Tang, *Chem. Soc. Rev.*, 2012, **41**, 1111–1129.
- 36 W. Huang, D. Restrepo, J. Y. Jung, F. Y. Su, Z. Liu, R. O. Ritchie, J. McKittrick, P. Zavattieri and D. Kisailus, *Adv. Mater.*, 2019, **31**, 1901561.
- 37 Z. Lin, Y. Liu, S. Raghavan, K. S. Moon, S. K. Sitaraman and C. P. Wong, *ACS Appl. Mater. Interfaces*, 2013, **5**, 7633–7640.
- 38 F. Ding, J. Liu, S. Zeng, Y. Xia, K. M. Wells, M. P. Nieh and L. Sun, *Sci. Adv.*, 2017, **3**, e1701212.
- 39 P. Das, S. Schipmann, J. M. Malho, B. Zhu, U. Klemradt and A. Walther, *ACS Appl. Mater. Interfaces*, 2013, **5**, 3738–3747.
- 40 P. Das, J. M. Malho, K. Rahimi, F. H. Schacher, B. Wang, D. E. Demco and A. Walther, *Nat. Commun.*, 2015, **6**, 1–14.
- 41 T. H. Lin, W. H. Huang, I. K. Jun and P. Jiang, *Chem. Mater.*, 2009, **21**, 2039–2044.
- 42 B. R. Furman, M. J. Rubal, C. K. Baker, C. N. Tiftickjian and S. T. Wellinghoff, *J. Mater. Sci.*, 2012, **47**, 6896–6907.
- 43 A. A. Verhoeff, R. P. Brand and H. N. W. Lekkerkerker, *Mol. Phys.*, 2011, **109**, 1363–1371.
- 44 S. E. Louaer, Y. Wang and L. Guo, *Mater. Chem. Phys.*, 2014, **148**, 1–4.
- 45 J. Zhang, J. Lee, Z. Wang, J. Yan, Z. Lu, S. Liu, D. Luo, K. Matyjaszewski and M. R. Bockstaller, *Polymer (Guildf.)*, 2017, **126**, 126–132.
- 46 X. Gu, L. Shaw, K. Gu, M. F. Toney and Z. Bao, *Nat. Commun.*, 2018, **9**, 1–16.
- 47 M. Mittal, R. K. Niles and E. M. Furst, *Nanoscale*, 2010, **2**, 2237–2243.
- 48 S. Louaer, Y. Wang and L. Guo, *ACS Appl. Mater. Interfaces*, 2013, **5**, 9648–9655.
- 49 T. Sugimoto, X. Zhou and A. Muramatsu, *J. Colloid Interface Sci.*, 2003, **259**, 43–52.
- 50 A. Sze, D. Erickson, L. Ren and D. Li, *J. Colloid Interface Sci.*, 2003, **261**, 402–410.
- 51 W. C. Oliver and G. M. Pharr, *J. Mater. Res.*, 2004, **19**, 3–20.
- 52 R. Saha and W. D. Nix, *Acta Mater.*, 2002, **50**, 23–38.
- 53 S. Sawamura, R. Limbach, H. Behrens and L. Wondraczek, *J. Non. Cryst. Solids*, 2018, **481**, 503–511.
- 54 M. Sebastiani, K. E. Johanns, E. G. Herbert, F. Carassiti and G. M. Pharr, *Philos. Mag.*, 2015, **95**, 1928–1944.
- 55 M. Wong, R. Ishige, K. L. White, P. Li, D. Kim, R. Krishnamoorti, R. Gunther, T. Higuchi, H. Jinnai, A. Takahara, R. Nishimura and H. J. Sue, *Nat. Commun.*, 2014, **5**, 1–12.
- 56 M. C. D. Mourad, D. V. Byelov, A. V. Petukhov, D. A. M. de Winter, A. J. Verkleij and H. N. W. Lekkerkerker, *J. Phys. Chem. B*, 2009, **113**, 11604–11613.
- 57 M. Le Berre, Y. Chen and D. Baigl, *Langmuir*, 2009, **25**, 2554–2557.
- 58 D. Kleshchanok, M. Heinen, G. Nägele and P. Holmqvist, *Soft Matter*, 2012, **8**, 1584–1592.
- 59 E. Rio and F. Boulogne, *Adv. Colloid Interface Sci.*, 2017, **247**, 100–114.
- 60 A. M. Wierenga, T. A. J. Lenstra and A. P. Philipse, *Colloids Surfaces A Physicochem. Eng. Asp.*, 1998, **134**, 359–371.
- 61 A. Gujral, K. A. O’Hara, M. F. Toney, M. L. Chabinyk and M. D. Ediger, *Chem. Mater.*, 2015, **27**, 3341–3348.
- 62 H. Bayesteh and A. A. Mirghasemi, *Soils Found.*, 2015, **55**, 1158–1170.
- 63 R. A. Chowdhury, M. Nuruddin, C. Clarkson, F. Montes, J. Howarter and J. P.

- Youngblood, *ACS Appl. Mater. Interfaces*, 2019, **11**, 1376–1383.
- 64 R. C. Shannon, B. Lafuente, R. D. Shannon, R. T. Downs and R. X. Fischer, *Am. Mineral.*, 2017, **102**, 1906–1914.
- 65 K. K. Phani and S. K. Niyogi, *J. Mater. Sci.*, 1987, **22**, 257–263.
- 66 H. Liu, J. Hu, J. Xu, Z. Liu, J. Shu, H. K. Mao and J. Chen, *Phys. Chem. Miner.*, 2004, **31**, 240–246.
- 67 V. Swamy and L. S. Dubrovinsky, *J. Phys. Chem. Solids*, 2001, **62**, 673–675.
- 68 J. H. Chu, L. B. Tong, J. B. Zhang, S. Kamado, Z. H. Jiang, H. J. Zhang and G. X. Sun, *Carbon N. Y.*, 2019, **141**, 154–168.
- 69 J. Y. Woo, J. H. Oh, S. Jo and C. S. Han, *ACS Nano*, 2019, **13**, 4522–4529.
- 70 T. Magrini, F. Bouville, A. Lauria, H. Le Ferrand, T. P. Niebel and A. R. Studart, *Nat. Commun.*, 2019, **10**, 1–10.
- 71 X. Zhang, P. L. Huestis, C. I. Pearce, J. Z. Hu, K. Page, L. M. Anovitz, A. B. Aleksandrov, M. P. Prange, S. Kerisit, M. E. Bowden, W. Cui, Z. Wang, N. R. Jaegers, T. R. Graham, M. Dembowski, H. W. Wang, J. Liu, A. T. N'Diaye, M. Bleuel, D. F. R. Mildner, T. M. Orlando, G. A. Kimmel, J. A. La Verne, S. B. Clark and K. M. Rosso, *ACS Appl. Nano Mater.*, 2018, **1**, 7115–7128.
- 72 J. A. Lefever, T. D. B. Jacobs, Q. Tam, J. L. Hor, Y.-R. Huang, D. Lee and R. W. Carpick, *Nano Lett.*, 2016, **16**, 2455–2462.
- 73 H. Zhang, D. R. Dunphy, X. Jiang, H. Meng, B. Sun, D. Tarn, M. Xue, X. Wang, S. Lin, Z. Ji, R. Li, F. L. Garcia, J. Yang, M. L. Kirk, T. Xia, J. I. Zink, A. Nel and C. J. Brinker, *J. Am. Chem. Soc.*, 2012, **134**, 15790–15804.
- 74 Q. Li, T. E. Tullis, D. Goldsby and R. W. Carpick, *Nature*, 2011, **480**, 233–236.
- 75 L. Zhang, G. Feng, Z. Zeravcic, T. Brugarcas, A. J. Liu and D. Lee, *ACS Nano*, 2013, **7**, 8043–8050.
- 76 L. An, D. Zhang, L. Zhang and G. Feng, *Nanoscale*, 2019, **11**, 9563–9573.
- 77 D. Zhang, Y. Xu, G. Feng, Y.-R. Huang and D. Lee, *J. Mater. Res.*, 2015, **30**, 3717–3727.
- 78 L. Zhang, J. H. Prosser, G. Feng and D. Lee, *Nanoscale*, 2012, **4**, 6543–6552.
- 79 M. Morits, T. Verho, J. Sorvari, V. Liljeström, M. A. Kostianen, A. H. Gröschel and O. Ikkala, *Adv. Funct. Mater.*, 2017, **27**, 1605378.
- 80 J. P. Best, J. Wehrs, M. Polyakov, M. Morstein and J. Michler, *Scr. Mater.*, 2019, **162**, 190–194.

Acknowledgement

This work was primarily supported by National Science Foundation CMMI-1662695. Partial support was provided by National Science Foundation via MRSEC DMR-1720530. We thank Dr. Jyo Lyn Hor for her assistance with the flow coating set-up, Aixi Zhang for her help with GIWAXS measurement and Dr. Haonan Wang for his suggestions on ellipsometry modelling.